Volume 10
Number 42
14 November 2022
Pages 15667–16158

Journal of Materials Chemistry C

Materials for optical, magnetic and electronic devices

rsc.li/materials-c

ISSN 2050-7526

ROYAL SOCIETY OF CHEMISTRY

PAPER

Philip J. Grandinetti *et al.*

Phase separation in alkali silicate glasses detected through inverse Laplace transform of ^{29}Si nuclear magnetic resonance echo train decay

Journal of Materials Chemistry C

ROYAL SOCIETY OF CHEMISTRY

PAPER

Cite this: J. Mater. Chem. C, 2022, 10, 15792

Phase separation in alkali silicate glasses detected through inverse Laplace transform of ^{29}Si nuclear magnetic resonance echo train decay†

Mark O. Bovee, ‡[a] Daniel Jardón-Álvarez, §[a] Deepansh Srivastava, ¶[a] Jingshi Wu[b] and Philip J. Grandinetti *[a]

Received 23rd August 2022,
Accepted 30th September 2022

DOI: 10.1039/d2tc03542a

rsc.li/materials-c

The ratio of silicon-29 nuclear magnetic resonance (NMR) coherence lifetimes for Q^4 and Q^3 sites under magic-angle spinning and a train of π pulses in a series of binary alkali silicate glasses is used to detect phase separation, even at small scales where the glass appears optically homogenous. This approach exploits the dependence of echo train coherence lifetimes on the residual heteronuclear dipolar coupling between Si-29 and the NMR active nuclei of neighboring network modifier cations. The shifted-echo phase incremented echo train acquisition NMR method is used to eliminate modulation of the echo train amplitudes due to *J* couplings across Si–O–Si linkages. A 2D Fourier and inverse Laplace transform of this dataset provides a correlation of the isotropic ^{29}Si chemical shift to echo train coherence lifetimes, giving a sensitive probe of phase separation as well as chemical composition and local structure of the different phases. The ^{29}Si Q^4:Q^3 mean coherence lifetime ratios are 28.8, 23.8, and 5.8 in the phase-separated glasses, $0.05Li_2O{\cdot}0.95SiO_2$, $0.1Li_2O{\cdot}0.9SiO_2$ and $0.05Na_2O{\cdot}0.95SiO_2$, respectively, while the ratio is reduced to 2.1, 1.6, and 1.6 in glasses not exhibiting signs of phase separation, $0.05K_2O{\cdot}0.95SiO_2$, $0.05Cs_2O{\cdot}0.95SiO_2$ and $0.10Cs_2O{\cdot}0.90SiO_2$, respectively. Phase separation inhibition, through addition of alumina, is also verified in $0.07Li_2O{\cdot}0.02Al_2O_3{\cdot}0.91SiO_2$.

1 Introduction

Phase separation in silicate glasses[1] can dramatically affect properties such as electrical conductivity, diffusion coefficients, viscosity, chemical durability, glass transition temperature, and light scattering. Recognizing the presence of phase separation and further predicting its occurrence in a given glass synthesis and composition is of fundamental importance for producing several technologically important materials.[2,3]

Phase separation forming spatial domains on the order of 200 nm or higher can be detected and studied with optical microscopy.[4] Finer scale phase separations at the level of microscopic and sub-microscopic domains (<200 nm), are more challenging to detect. Such small-scale phase separation can occur when high viscosity within the immiscibility dome inhibits the growth of larger domains. This effect is particularly enhanced in the case of metastable immiscibility.[5] While direct transmission electron microscopy (TEM)[6] is capable of probing as far down as 0.05 nm, it requires extremely thin specimens on the order of 100 nm, which can be difficult to prepare and can also lead to fatal flaws in the sample. As an alternative, a thin carbon film is deposited on the glass surface to create a surface replica. This film, shadowed with a heavy metal, is removed by etching and examined by TEM to obtain a replica micrograph of the surface. Sample preparation is less challenging with Scanning Electron Microscopy (SEM), although it has a lower resolution (between 0.5 and 4 nm) than TEM.[7] Atomic force microscopy (AFM) has also been proposed as an inexpensive approach for determining microstructures of phase-separated glasses with a resolution down to 50 nm.[8] Alternatively, small-angle X-ray scattering (SAXS)[9,10] can be used to detect phase separation at these smaller length scales. In SAXS, an analysis of the diffuse profile as a function of the scattering angle can provide information

[a] Department of Chemistry, The Ohio State University, 120 W. 18th Avenue, Columbus, Ohio 43210-1173, USA. E-mail: grandinetti.1@osu.edu
[b] Science & Technology Division, SP-FR-05, Corning Research and Development Corporation, Corning, NY 14831, USA

† Electronic supplementary information (ESI) available: Background NMR theory of residual dipolar couplings, the best-fit parameters obtained from the least-squares analysis of the spectra in Fig. 2, photographs of 5Na:95Si, 5Li:95Si, and 10Li:90Si glasses, X-ray diffraction data of the 5Li:95Si and 10Li:90Si glasses, and the parameters for the inverse Laplace transforms of the experimental datasets. See DOI: https://doi.org/10.1039/d2tc03542a

‡ Present address: Chemistry Division, Naval Research Laboratory, Washington, DC 20375, USA.
§ Present address: Department of Molecular Chemistry and Materials Science, Weizmann Institute of Science, Rehovot, 76100, Israel.
¶ Present address: Hyperfine, Inc., Guilford, CT, USA.

regarding the size and distribution of the heterogeneities and hence the microstructure.

Unfortunately, the techniques mentioned above provide little to no information on the composition and atomic-level structure of the phase-separated regions. It has long been known that a combination of nuclear magnetic resonance (NMR) spectroscopy and relaxometry in silicate glasses can detect the presence of phase separation through differential longitudinal relaxation rates as well as provide insight into the structural variations in different phase-separated domains through spectroscopically resolved resonances.[11–15] This differential longitudinal relaxation arises from the presence of small amounts of paramagnetic cations,[16,17] intentionally or unintentionally added into the silica network, which distribute preferentially in the modifier-cation-rich (depolymerized) regions. The ^{29}Si nuclei in those regions rich in paramagnetic cations have faster nuclear relaxation rates—a consequence of the large magnetic field fluctuations emanating from the paramagnetic sites. This differential paramagnetic relaxation enhancement can create a strong contrast among spin 1/2 nuclei, like ^{29}Si, where other nuclear spin relaxation mechanisms in the glass are orders of magnitude weaker. In the absence of paramagnetic impurities, ^{29}Si longitudinal relaxation times in glasses are known to be on the order of days.[18] Thus, the fluctuating magnetic fields from paramagnetic impurities, even at long distances, can still dominate the longitudinal relaxation of ^{29}Si nuclei. It has further been claimed by Devreux *et al.*[19] that fitting the initial ^{29}Si longitudinal magnetization recovery to a power-law can be used to determine the silicon mass fractal dimension in a silicate glass. This analysis is restricted to the initial magnetization recovery as it assumes that a single paramagnetic center causes relaxation. As a result, this approach excludes any information on longer distances associated with the more slowly relaxing nuclei. This approach also has been used by others[11–15,20] to suggest that differences in these mass fractal dimensions can be used to identify clustering and phase separation.

In this paper, we propose exploiting the differential coherence lifetimes of the ^{29}Si magnetization under MAS and a π-pulse train caused by the presence of alkali modifier cations to detect phase separation. This approach does not require the addition of paramagnetic impurities and the assumption that paramagnetic ions differentially segregate into the regions with high modifier cation content. In a recent investigation, we have shown that the nuclear magnetic properties of modifier cations play a significant role in determining ^{29}Si coherence lifetimes, leading to differences as large as three orders of magnitude.[21] In compositions with abundant NMR active nuclei, such as alkali silicates, the ^{29}Si coherence lifetimes are dominated by coherent dephasing due to residual heteronuclear dipolar couplings. This homogeneous broadening is not completely removed with a π pulse train under magic-angle spinning (MAS). Thus, while MAS still resolves resonances of structurally distinct sites, the differential coherence lifetimes during a π-pulse echo train signal can detect the presence of phase separation, that is, differentiate between phases of high and low modifier content, whenever these modifiers have abundant NMR active nuclei.

To investigate the potential of using differential coherence lifetimes as a probe of phase separation in binary silicate glasses, we determined the π-pulse echo train coherence lifetimes of ^{29}Si in lithium, sodium, potassium, and cesium silicate glasses with low modifier cation content (between 5 and 10%) as well as analog samples to which small amounts of alumina were added. These glasses were chosen as the tendency towards immiscibility in binary alkali silicate glasses increases with increasing modifier cation potential;[22] thus, lithium and sodium silicates show a high tendency to phase segregate. While the possibility of phase separation in potassium silicates is still controversial,[23–26] phase separation is not expected for alkali cations heavier than potassium.[27] Small amounts of alumina reduce the tendency towards phase separation by lowering the critical temperature and increasing the glass transition temperature.[13,27,28]

All glasses commonly present a wide distribution of coherence lifetimes, reflecting the continuous distribution of environments in a structure lacking long-range structural order. To better quantify the distribution of coherence lifetimes, we employ an inverse Laplace transform[29] (ILT) as it provides a more quantitative and less restrictive analysis compared to a multi- or stretched exponential model.

Finally, one complication with this approach is that, even at natural abundance levels of ^{29}Si (4.7%), there will be a small but noticeable modulation of the echo train signal from isolated geminal J couplings between ^{29}Si across a bridging oxygen linkage.[30,31] Since π-pulses do not refocus J couplings, measuring coherence lifetimes in the presence of J couplings will cause oscillations of the decay, hindering a precise analysis of the distribution of coherence lifetimes. To overcome this problem, we employ a pulse sequence, based on previous work,[31] that allows the coherence lifetimes to be measured without substantial contamination from J coupling oscillations.

2 Methods

2.1 Silica glass preparation

A series of highly siliceous alkali silicate glasses with compositions given in Table 1 were prepared in the Advanced Materials Processing Lab at Corning Inc. Adding the alkali oxides to a silica melt causes depolymerization of the silicate network. This depolymerization leads to the formation of five types of SiO_4 tetrahedra, each characterized by its connectivity, *i.e.*, the number of oxygen that are corner-linked to other tetrahedra.[32,33] These are designated with the notation Q^n, where $n(\sim 0–4)$ represents the number of bridging oxygen per tetrahedron. In peralkaline ternary compositions $n_M M_2O{\cdot}n_{Al}Al_2O_3{\cdot}n_{Si}SiO_2$ where $n_{Al}/n_M \leq 2$ and $n_{Al}/n_{Si} \leq 1$ the Al enters the network as negatively charged AlO_4 along with a proportionate reduction in NBO, *i.e.*, Q^3 sites. In a homogeneous glass, the alkali cations act to charge compensate the AlO_4 and, if $n_{Al}/n_M < 2$, to depolymerize the network and charge compensate the NBO.[34–40] The presence of alumina is known to reduce the tendency of silicate glasses to phase separate.

The batch materials are industrial quality sand, alumina, and alkali carbonates. The glasses were melted in a 2 kg batch

Table 1 Sample compositions, melt temperatures, and times of silicate glasses studied. Each glass was melted twice in 2 kg batches at 1650 °C for the durations specified above in Pt/Rh crucibles. Quenching for the first melt was performed by pouring it into cold water and allowing the resulting glass to dry overnight. The second melt was quenched by pouring it onto a steel plate to form a glass patty, which was then annealed overnight at 500 °C or 600 °C to reduce thermal stress

Sample	Composition	Melt procedure
5Li:95Si	$0.05Li_2O{\cdot}0.95SiO_2$	1650 °C (2 × 6 h)
10Li:90Si	$0.10Li_2O{\cdot}0.90SiO_2$	1650 °C (2 × 6 h)
7Li:2Al:91Si	$0.07Li_2O{\cdot}0.02Al_2O_3{\cdot}0.001SnO_2{\cdot}0.91SiO_2$	1650 °C (1 × 6 + 1 × 4 h)
5Na:95Si	$0.05Na_2O{\cdot}0.95SiO_2$	1650 °C (2 × 6 h)
5K:95Si	$0.05K_2O{\cdot}0.95SiO_2$	1650 °C (2 × 6 h)
5Cs:95Si	$0.05Cs_2O{\cdot}0.95SiO_2$	1650 °C (2 × 6 h)
10Cs:90Si	$0.10Cs_2O{\cdot}0.9SiO_2$	1650 °C (2 × 6 h)
7Cs:2Al:91Si	$0.07Cs_2O{\cdot}0.02Al_2O_3{\cdot}0.001SnO_2{\cdot}0.91SiO_2$	1650 °C (1 × 6 + 1 × 4 h)

in Pt/Rh crucibles at 1650 °C twice to achieve better homogeneity. A small amount of alumina was added to two compositions to reduce phase separation. Tin(IV) oxide was also added to these glasses as a fining agent. Note that no paramagnetic oxides were added to enhance ^{29}Si spin–lattice relaxation times. The first melt was poured into cold water to cool; then, the glass cullet was dried overnight to remove water. After the second melt, the melts were poured on a steel plate to form glass patties. The glass patties were annealed at 500 °C or 600 °C overnight to reduce thermal stress. Except for the 10Li:90Si composition (as seen in Fig. S1, ESI†), all samples were optically clear, showing no signs of opalescence. X-ray diffraction measurements on the 5Li:95Si and 10Li:90Si glasses show a small fraction of cristobalite crystallization in the 10Li:90Si composition.

Flame Emission Spectroscopy (FES) was used to quantify alkali oxides for both binary and ternary glasses. For ternary glasses, alumina content was measured *via* Inductively Coupled Plasma Optical Emission Spectroscopy (ICP-OES), and silica content was quantified *via* gravimetric analysis. Chemical composition analysis showed that target compositions were obtained within an error margin of 0.1 mol%.

The synthesized high silica glasses were analyzed with Scanning Electron Microscopy (SEM) using a Hitachi SU-70 microscope. To reduce charging, samples were fractured and etched with 1% HF and coated with conducting carbon.

2.2 NMR spectroscopy

Glass samples were ground and packed in NMR rotors under inert conditions in a nitrogen-filled glove box. Longitudinal nuclear magnetic recoveries were measured on a hybrid Tecmag Apollo-Chemagnetics CMX II 9.4 T NMR spectrometer using a 4 mm Chemagnetics MAS probe spinning at $\omega_R/(2\pi)$ = 10 kHz. Echo train coherence lifetimes were measured on a Bruker Avance III HD 9.4 T NMR spectrometer using a 7 mm Bruker MAS probe and at a spinning speed of $\omega_R/(2\pi)$ = 7 kHz. The stability of the spinning speed was 2 Hz. The magic angle was set with the ^{2}H signal of deuterated hexamethylbenzene. All measurements were done at room temperature.

2.2.1 Longitudinal magnetization recovery. Longitudinal nuclear magnetization recoveries were measured using the saturation recovery sequence[41] with logarithmically spaced time delays. ^{133}Cs signal was detected with a Hahn echo,[42] while all other nuclei were detected after single-pulse excitation. In these measurements, the π/2 pulse lengths for ^{29}Si were 7.5 μs. For ^{7}Li and ^{133}Cs, all NMR transitions were excited with π/2 pulse lengths of 7 μs and 5 μs, respectively. The longitudinal magnetization recovery was fit to the stretched exponential function,

$$M_z(t) = M_z(\infty)\cdot[1 - \exp[-(t/T_1)^{\beta_1}]], \quad (1)$$

where T_1 is the longitudinal magnetization recovery time, and β_1 is the Kohlrausch exponent. The stretched exponential function accounts for a distribution of T_1 times. The best-fit parameters are given in Table 2. With no paramagnetic doping, the exceptionally long ^{29}Si T_1 times, which exceeded 1000 s in all samples, prevented a complete recovery of the longitudinal component of the ^{29}Si magnetization from being measured. Nonetheless, the longitudinal recoveries of ^{29}Si Q^3 sites were observed to be distinctly faster than those of Q^4 sites in the phase-separated glasses. This is consistent with previous studies of ^{29}Si longitudinal relaxation in phase-separated silicate glasses.[11–13,15,43]

2.2.2 NMR π-echo train decay and modulation. The ^{29}Si π/2 and π pulse lengths for echo train measurements were 4.6 μs and 9.2 μs, respectively. All experiments were preceded by a saturation pulse train and a recycle delay of 1000 s. Since this delay does not ensure the total recovery, the Q^3/Q^4 ratios obtained from integrated amplitudes may not be quantitative.

Measuring a π-pulse echo train lifetime with the Carr–Purcell–Meiboom–Gill (CPMG) sequence is complicated by rf inhomogeneities, which introduce stimulated echoes whose decay is governed by a mix of longitudinal and transverse relaxation. Therefore, we employ a variant of the Phase Incremented Echo Train Acquisition[31,44] (PIETA) sequence, illustrated in Fig. 1,

Table 2 ^{29}Si, ^{7}Li, ^{23}Na and ^{133}Cs T_1 relaxation time parameters. Parameter uncertainties are given as one standard deviation

Sample	Nucleus	T_1/s	β_1
10Li:90Si	^{29}Si (Q^4)	$>10^4$	—
10Li:90Si	^{29}Si (Q^3)	~1500	—
5Li:95Si	^{7}Li	2.3 ± 0.1	0.85 ± 0.04
10Li:90Si	^{7}Li	2.2 ± 0.1	0.93 ± 0.04
7Li:2Al:91Si	^{7}Li	2.4 ± 0.1	0.92 ± 0.04
5Na:95Si	^{23}Na	0.085 ± 0.001	0.49 ± 0.01
5Cs:95Si	^{133}Cs	60 ± 10	0.56 ± 0.03
10Cs:90Si	^{133}Cs	15 ± 2	0.64 ± 0.03
7Cs:2Al:91Si	^{133}Cs	46 ± 5	0.59 ± 0.02

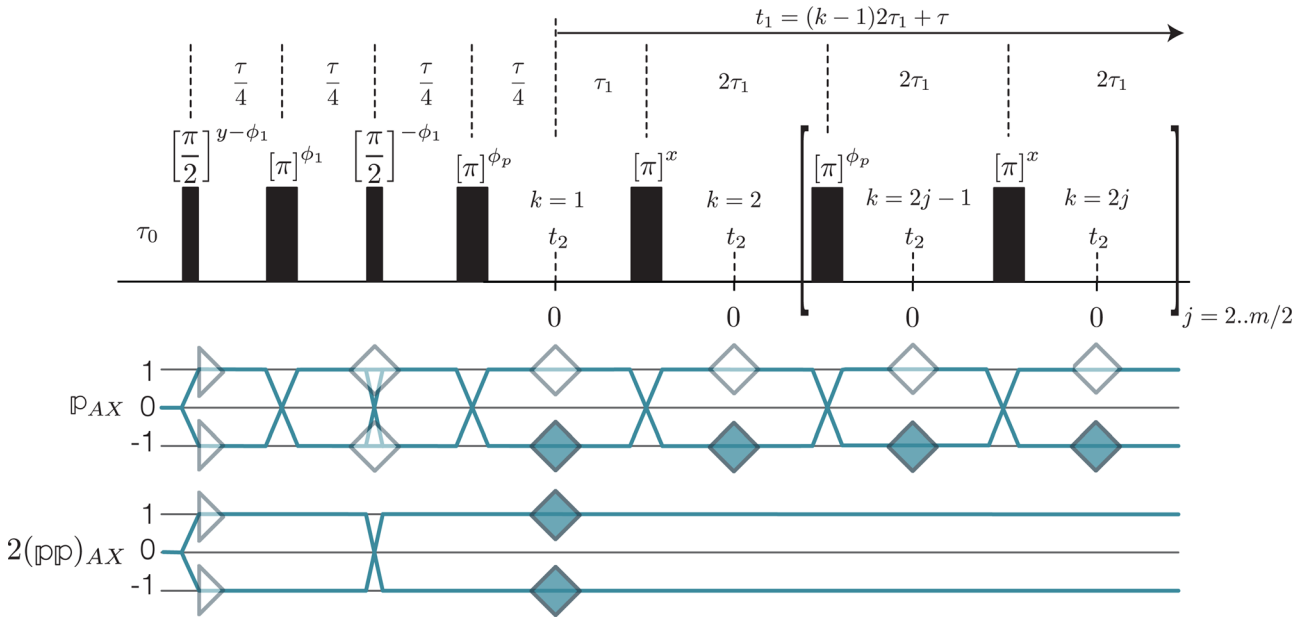

Fig. 1 Graphical representation of the SE-PIETA sequence[31] with relevant symmetry pathways.[45] In this sequence, ϕ_p is the PIETA phase dimension, k is the echo count dimension, and t_2 is the direct acquisition (chemical shift) dimension. The sequence includes an echo shift dimension, τ. The number of loops for $j = 2..m/2$ gives a k dimension with m samples. The PIETA phase ϕ_p dimension is incremented from 0 to 2π in steps of $2\pi/m$. After a Fourier transform along ϕ_p, the desired accumulated Δp are selected to reduce the signal to $S(\tau,k,t_2)$, respectively. The k dimension is converted into the echo decay dimension, t_1, according to $t_1 = (k-1)2\tau_1 + \tau$. An 8-step phase cycle was used for ϕ_1. The signal was sampled non-uniformly along τ with the values given in Table 3. A Fourier transform of the signal along t_2 followed by an inverse Laplace transform along t_1 yields a 2D spectrum correlating the MAS resonances with their λ^{-1} decay times. To avoid spinning sideband artifacts, the spacing between the centers of adjacent pulses should be an integer multiple of the rotor period.

which eliminates these stimulated echo artifacts and provides a more accurate measure of the spin-echo decay and any J coupling modulations. Additional details on its implementation and signal processing are given in the caption of Fig. 1.

In silicate glasses, the ^{29}Si echo train amplitude can be modulated by J couplings across ^{29}Si–O–^{29}Si linkages, even at ^{29}Si natural abundance.[21,31] When there is a weak J coupling between dilute ^{29}Si–^{29}Si pairs under fast magic-angle spinning (MAS) the transition frequency is given by

$$\Omega_{AX} = \omega_0(1 - \sigma_{iso,A})\mathbb{P}_A + \omega_0(1 - \sigma_{iso,X})\mathbb{P}_X - 2\pi J_{AX}(\mathbb{PP})_{AX}, \quad (2)$$

where the transition symmetry functions are given by

$$\mathbb{P}_A = m_{A,j} - m_{A,i},$$

$$\mathbb{P}_X = m_{X,j} - m_{X,i},$$

$$(\mathbb{PP})_{AX} = m_{A,j}m_{X,j} - m_{A,i}m_{X,i}. \quad (3)$$

Here $\sigma_{iso,A}$ and $\sigma_{iso,X}$ are the isotropic nuclear shieldings, ω_0 is the Larmor frequency and J_{AX} is the indirect coupling constant. The quantum numbers, m_A and m_X, are associated with quantized energy levels of A and X nuclei, respectively, while i and j represent the initial and final energy states of the NMR transition. In the case of two weakly coupled homonuclear nuclei it is useful to define the additional transition symmetry function $\mathbb{P}_{AX} = \mathbb{P}_A + \mathbb{P}_X$.

One approach to suppress echo modulation from J couplings and measure only the spin echo decay is to generate a train of simultaneous $\mathbb{P}_{AX}$ and $(\mathbb{PP})_{AX}$ echoes, *i.e.*, total echoes, which refocus both chemical shift and J coupling evolution, with the sequence[31,46–48]

$$\frac{\pi}{2} - \left[\frac{\tau}{4} - \pi - \frac{\tau}{4} - \frac{\pi}{2} - \frac{\tau}{4} - \pi - \frac{\tau}{4} \rightarrow \bullet\right]_{j=1\ldots m}.$$

In practice, introducing a phase cycle in this sequence to avoid contaminations from stimulated echoes would lead to prohibitively long measurements, as every additional total echo requires an additional nested 8-step phase cycle.[31] Here we adopt an intermediate approach, using the shifted-echo PIETA sequence,[31] shown in Fig. 1, which acquires the first echo as simultaneous $\mathbb{P}_{AX}$ and $(\mathbb{PP})_{AX}$ echoes followed by a train of $\mathbb{P}_{AX}$ echoes. A detailed explanation of the symmetry pathways in the SE-PIETA sequence is provided by Srivastava *et al.*[31] By varying τ in successive measurements, the initial echo decay can be finely sampled on the first (simultaneous $\mathbb{P}_{AX}$ and $(\mathbb{PP})_{AX}$) echo without J coupling modulations. The J coupling modulations begin only at the start of the $\mathbb{P}_{AX}$ echo train where $t_1 = \tau$. The short-lived J coupling modulations can be skipped over using a sufficiently long $2\tau_1$. Between the first simultaneous $\mathbb{P}_{AX}$ and $(\mathbb{PP})_{AX}$ echo and the next $\mathbb{P}_{AX}$ only echo; however, there is a small step in the overall decay due to the loss of the dephased J-coupled ^{29}Si nuclei. Careful choice of the parameters τ and $2\tau_1$ enable the measurement of a wide range of coherence lifetimes, which is particularly important in phase-separated glasses where a wider

Table 3 The delay combinations of τ and $2\tau_1$ used in the SE-PIETA pulse sequence shown in Fig. 1. The remaining SE-PIETA acquisition parameters were the same in all experiments with τ_0 = 1000 s and $m \times n_{t_2} \times n_{\phi_p}$ = 8 × 512 × 10, leading to a total experimental time of 22.2 × 3 = 66.6 h for all samples except 7Li:2Al:91Si, which was acquired in 22.2 × 4 = 88.8 h, where m is the number of echoes, n_{t_2} is the number of acquisition points, n_ϕ is the number of phases in the phase dimension

Sample	τ/ms	$2\tau_1$/ms
5Li:95Si	6.28	259.14
	12.56	646.28
	37.72	3090.96
10Li:95Si	6.28	259.14
	12.56	646.28
	37.72	3090.96
7Li:1Al:91Si	6.28	259.14
	12.56	262.28
	37.72	274.86
	100.56	306.28
5Na:95Si	6.28	259.14
	12.56	646.28
	37.72	3090.96
5K:95Si	6.28	259.14
	12.56	646.28
	37.72	3090.96
5Cs:95Si	6.28	259.14
	12.56	646.28
	37.72	3090.96
10Cs:95Si	6.28	259.14
	12.56	262.28
	37.72	274.86
7Cs:2Al:91Si	6.28	259.14
	12.56	262.28
	37.72	274.86

range of ^{29}Si coherence lifetimes may be present in the glass. The SE-PIETA acquisition parameters for all compositions measured are given in Table 3.

With suppression of the J coupling modulation, the ^{29}Si echo train coherence decay in a silicate glass is given by

$$s(t) = \int_\lambda p(\lambda)\exp(-\lambda t)\mathrm{d}\lambda, \tag{4}$$

where $p(\lambda)$ is the probability distribution of echo train coherence decay rate constants, λ, present in the glass. An inverse Laplace transform (ILT)[49,50] along an echo train decay can be used to obtain the distribution of exponential echo decay rate constants, λ. Alternatively, the ILT kernel can be redesigned to obtain $p(\lambda^{-1})$, the probability distribution of echo train coherence lifetimes, λ^{-1}, present in the glass, *i.e.*,

$$s(t) = \int_{\lambda^{-1}} p\left(\lambda^{-1}\right)\exp\left(-t/\lambda^{-1}\right)\mathrm{d}\lambda^{-1}. \tag{5}$$

Details on the numerical implementation of the Inverse Laplace Transform (ILT) algorithm with l_1 regularization,[51–59] employed in this study, are given in Appendix A. All inversions were performed using the open-source Python package *mrinversion*.[60,61] The Python Jupyter notebooks for performing the inversion of all experimental datasets in this study are available in the ESI.†

The ^{29}Si echo train coherence decay lifetimes, λ^{-1}, under MAS are dominated by coherent dephasing due to residual heteronuclear magnetic dipolar couplings to nearby NMR active nuclei.[21] In Section S1 of the ESI† and elsewhere,[21] we show that these couplings are not completely removed by magic-angle spinning due to the strong homonuclear dipolar couplings among the NMR active nuclides of the alkali cations. The magnitude of this residual heteronuclear dipolar interaction is given by

$$\frac{\omega_\mathrm{d}^\mathrm{II}\omega_\mathrm{d}^\mathrm{IS}}{\omega_\mathrm{R}} = \frac{1}{\omega_\mathrm{R}}\cdot\left(\frac{\mu_0}{4\pi}\right)^2\cdot\frac{{\gamma_\mathrm{I}}^2\hbar}{{r_\mathrm{II}}^3}\cdot\frac{\gamma_\mathrm{I}\gamma_\mathrm{S}\hbar}{{r_\mathrm{IS}}^3}. \tag{6}$$

Here, we have defined

$$\omega_\mathrm{d}^\mathrm{II} = -\frac{\mu_0}{4\pi}\frac{{\gamma_\mathrm{I}}^2\hbar}{{r_\mathrm{II}}^3} \tag{7}$$

as the homonuclear dipolar coupling constant, where γ_I is the nuclear magnetogyric ratio for the quadrupolar nuclide of the alkali cation, and r_II is the distance between alkali cations. Similarly, we have defined

$$\omega_\mathrm{d}^\mathrm{IS} = -\frac{\mu_0}{4\pi}\frac{\gamma_\mathrm{I}\gamma_\mathrm{S}\hbar}{{r_\mathrm{IS}}^3} \tag{8}$$

as the heteronuclear dipolar coupling constant, where γ_S is the nuclear magnetogyric ratio for ^{29}Si, and r_IS is the distance between ^{29}Si and the NMR active nuclei of the alkali cations. While these residual dipolar couplings are progressively removed with increasing MAS speeds, as seen in eqn (6), they remain the dominant dephasing mechanism of the ^{29}Si echo-train well beyond the MAS speeds needed to obtain high-resolution ^{29}Si MAS spectra.[21] Therefore, the key factors to consider when interpreting the variations in the ^{29}Si coherence lifetime distributions in the alkali silicate glasses are the size of the gyromagnetic ratio for the quadrupolar nuclei of the alkali cation, the distance between alkali cations, and the distance between the alkali cations and the ^{29}Si nuclides. This is why the ^{29}Si echo-train coherence lifetimes are particularly sensitive to phase separation since the stronger homonuclear dipolar couplings between alkali nuclides in the alkali-rich phases "amplify" the heteronuclear dipolar coupling to ^{29}Si in this cross-term between the two couplings. The $\gamma_\mathrm{I}\hbar$ factors in units of nuclear magnetons of the most abundant NMR-active nuclei in the glass compositions of this study are given in Table 4. In a non-phase separated sample where modifier cations are distributed homogeneously, one would expect all Q^n sites to be in relative proximity to the modifier cations and have similar coherence lifetime distributions. In the discussion that follows, we will also use the ratio of the mean coherence lifetimes for Q^4 and Q^3, *i.e.*,

$$r_\lambda = \lambda^{-1}_\mathrm{mean}(\mathrm{Q}^4)/\lambda^{-1}_\mathrm{mean}(\mathrm{Q}^3), \tag{9}$$

as a simple indicator of phase separation.

Table 4 The $\gamma_\mathrm{I}\hbar$ values of the most abundant NMR-active nuclei in the glass compositions of this study. Here, μ_N is the nuclear magneton

Isotope	Abundance/%	$\gamma_\mathrm{I}\hbar/\mu_\mathrm{N}$
^{7}Li	92.41	2.171
^{23}Na	100	1.478
^{27}Al	100	1.457
^{39}K	93.2581	0.261
^{133}Cs	100	0.738

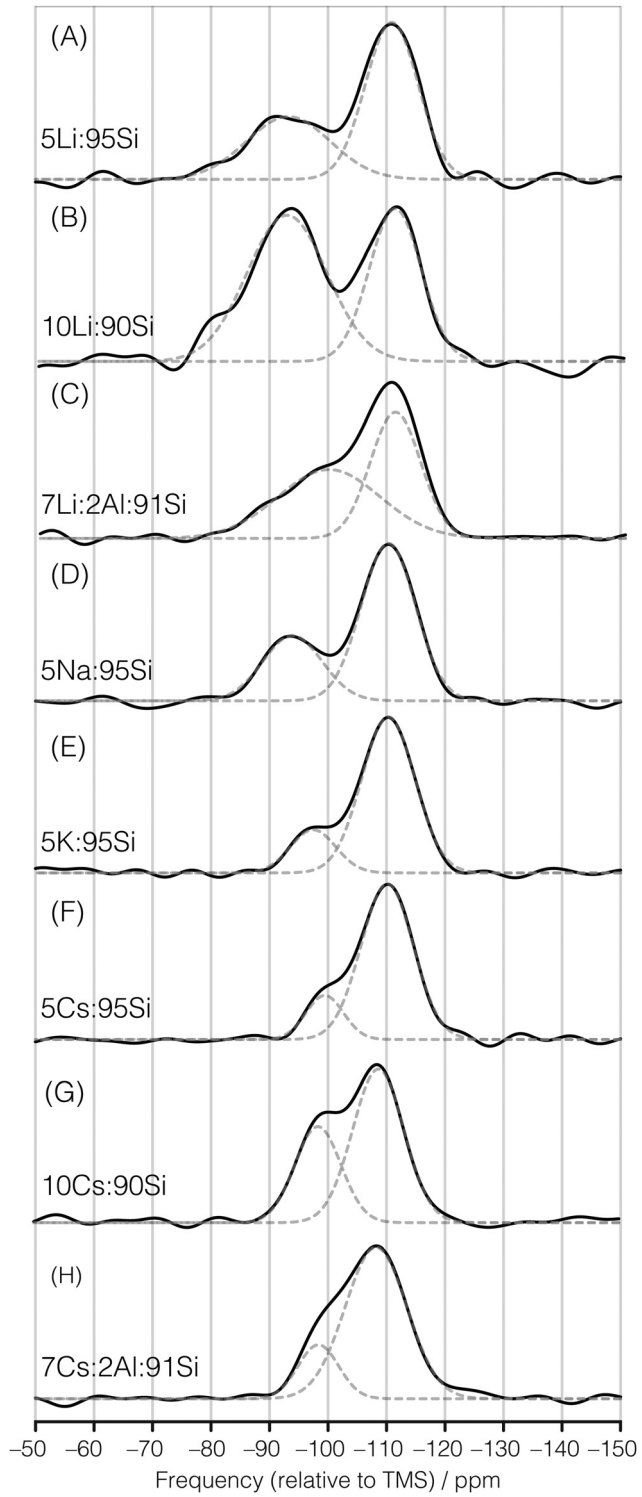

Fig. 2 ^{29}Si magic-angle spinning spectra (solid black lines) of the first echo of each measurement along with best-fit Q^3 and Q^4 Gaussian line shapes (dashed lines) for the compositions (A) 5Li:95Si, (B) 10Li:90Si, (C) 7Li:2Al:91Si, (D) 5Na:95Si, (E) 5K:95Si, (F) 5Cs:95Si, (G) 10Cs:90Si, and (H) 7Cs:2Al:91Si. Frequencies in ppm are referenced to TMS. Additional details of the least-squares analysis, along with other best-fit parameters, are given in Table S1 of the ESI.†

The modes of the chemical shift distributions for the Q^3 and Q^4 sites were determined by fitting the isotropic 1D spectrum of the first echo of each measurement to two Gaussian line shapes, as shown in Fig. 2. The solid line represents the 1D isotropic spectrum of each sample's first echo. Additionally, the dashed lines represent the best-fit Gaussian line shapes for the Q^3 and Q^4 sites. It should be noted that the relative populations of Q^3 to Q^4 sites cannot be gained from integrated areas due to bias caused by differential echo train coherence lifetimes. Nonetheless, the MAS spectra were analyzed to determine the modes of Q^3 and Q^4 site chemical shift distributions given in Table 5.

3 Results and discussion

3.1 Cesium silicate glasses

As the cesium silicate glasses do not phase separate, even at the lower Cs_2O content glasses in this study, we can expect a homogeneous distribution of Cs^+ cations in all three cesium silicate glass compositions. Thus, we begin our discussion with these compositions to illustrate the behavior of ^{29}Si MAS echo-train coherence lifetimes in a non-phase separated glass as a function of changing composition.

First, we note that the one-dimensional ^{29}Si MAS spectra of the three cesium glass compositions, shown in Fig. 2(F)–(H), can be decomposed into two broad resonances associated with Q^4 sites around −110 ppm and Q^3 sites around −99 ppm. There are two established NMR parameter–structure relationships that explain how the width of the Q^4 and Q^3 isotropic chemical shift distributions arise from structural distributions in the glass. First, there is an approximately linear relationship between chemical shift on the mean Si–O–Si angle between Q^n sites causing the chemical shift to increase (less shielding) with decreasing mean Si–O–Si angle.[62–64] This effect explains, at best, a width of no more than ∼6 ppm, assuming the mean Si–O–Si angle varies between 150° and 140°. The second structural variation broadening the Q^4 and Q^3 resonances is a shift to less negative chemical shifts as the neighboring tetrahedra[15,65] change from Q^4 to Q^3. For example, starting from silica-rich compositions and increasing the Cs content, the predominant Q^4 sites change from $Q^{4,4444}$ to $Q^{4,4443}$ to $Q^{4,4433}$ to $Q^{4,4333}$ to $Q^{4,3333}$. Here the notation $Q^{4,4444}$ represents a Q^4 connected to four other Q^4, as in silica glass SiO_2, while $Q^{4,4333}$ represents a Q^4 connected to one Q^4 and three Q^3. Similarly, there is an increase in the Q^3 chemical shift with increasing Cs content arising from a shifting predominance of anionic clusters from $Q^{3,444}$ to $Q^{3,443}$ to $Q^{3,433}$ to $Q^{3,333}$.[66]

This variation of neighboring tetrahedra of a Q^n also explains the distributions of Q^4 and Q^3 coherence lifetimes in the 2D FT-ILT spectra of a ^{29}Si SE-PIETA NMR measurement of the cesium silicate glasses. In the 2D FT-ILT of the 5Cs:95Si glass, shown in Fig. 3(A), we observe that the ^{29}Si MAS echo-train coherence lifetimes span two orders of magnitude. This is due to a distribution of residual heteronuclear dipolar couplings between the ^{29}Si and ^{133}Cs nuclei, which in turn, is a result of the variation of neighboring tetrahedra of a Q^n. That is, the longest coherence lifetime is associated with $Q^{4,4444}$, and the coherence lifetime decreases with increasing coordination by Q^3

Table 5 ^{29}Si most probable chemical shifts and coherence lifetimes of the Q^3 and Q^4. The ratio r_λ is defined in eqn (9) as the ratio of the mean coherence lifetimes. For compositions marked with an asterisk, Q^3 and Q^4 sites were resolved in the 2D ILT-FT spectrum and the 2D ILT-FT spectrum was used to determine the $\lambda^{-1}_{mode}(Q^3)$ and $\lambda^{-1}_{mode}(Q^4)$. The Q^3 and Q^4 sites were not resolved in the 2D ILT-FT spectrum of the remaining compositions and $\lambda^{-1}_{mode}(Q^3)$ and $\lambda^{-1}_{mode}(Q^4)$ were determined from the ILT cross-sections taken at the $\delta_{mode}(Q^3)$ and $\delta_{mode}(Q^4)$ values determined by the least-squares analysis of the MAS spectra in Fig. 2

Sample	$\delta_{mode}(Q^4)$/ppm	$\lambda^{-1}_{mode}(Q^4)$/ms	$\lambda^{-1}_{mean}(Q^4)$/ms	$\delta_{mode}(Q^3)$/ppm	$\lambda^{-1}_{mode}(Q^3)$/ms	$\lambda^{-1}_{mean}(Q^3)$/ms	r_λ
5Li:95Si*	−111.5	862.0	1343.8	−93.5	38.1	46.6	28.8
10Li:90Si*	−109.0	181.2	837.3	−91.9	38.1	35.1	23.8
7Li:2Al:91Si	−110.7	107.7	128.7	−99.3	38.1	42.3	3.0
5Na:95Si*	−110.7	181.2	367.7	−94.4	107.7	63.5	5.8
5K:95Si*	−109.8	304.7	315.7	−98.4	181.2	151.4	2.1
5Cs:95Si	−110.1	512.5	316.1	−99.4	181.2	192.1	1.6
10Cs:90Si	−108.9	181.2	157.6	−98.6	107.7	100.6	1.6
7Cs:2Al:91Si	−108.2	181.2	181.2	−98.4	181.2	104.4	1.7

sites, *i.e.*, decreasing from $Q^{4,4444}$ to $Q^{4,4443}$ to $Q^{4,4433}$ to $Q^{4,4333}$ to $Q^{4,3333}$. Similarly, the ^{29}Si lifetimes are longest for $Q^{3,444}$, and decrease progressively from $Q^{3,444}$ to $Q^{3,443}$ to $Q^{3,433}$ to $Q^{3,333}$. We also observe in Fig. 3(A) that the Q^4 coherence lifetime distribution is slightly wider than the Q^3 distribution. While both distributions share the same lower limit, the Q^4 lifetimes extend to slightly higher values than Q^3. This is expected since the cesium cations are further away from the $Q^{4,4444}$ sites than the $Q^{3,444}$ sites.

The 2D FT-ILT of the 10Cs:90Si glass is shown in Fig. 3(C). Here, we observe that the increased cesium content of the 10Cs:90Si glass relative to the 5Cs:95Si glass leads to less-negative chemical shifts for the Q^4 and Q^3 sites, along with a clear shift of both sites to lower coherence lifetimes. Both observations are a result of a reduction in the $Q^{4,4444}$ and $Q^{3,444}$ populations and a commensurate increase in the other $Q^{4,ijkl}$ and $Q^{3,ijk}$ populations.

From a least-squares fit of the ^{29}Si MAS spectra of the 5Cs:95Si and 10Cs:90Si glasses, shown in Fig. 2(F) and (G), we determine the modes of the Q^4 and Q^3 chemical shift distributions given in Table 5. Cross-sections as a function of coherence lifetime taken at the respective modes of the Q^4 and Q^3 chemical shift distributions are shown in Fig. 3(B) and (D). Using the mean Q^4 and Q^3 lifetimes from these cross-section we obtain a ratio of r_λ = 1.6 for both the 5Cs:95Si and 10Cs:90Si glasses. Finding $r_\lambda > 1$, *i.e.*, a mean longer coherence lifetime for Q^4 compared to Q^3, is not unexpected even in a non-phase separated homogenous glass due to the lower residual heteronuclear dipolar couplings of the $Q^{4,4444}$ sites.

As mentioned earlier, adding alumina is known to reduce the tendency of silicate glasses to phase separate. The addition of alumina decreases the relative population of the Q^3 sites, with cesium cations charge compensating the negatively charged AlO_4 and remaining Q^3 sites in the network. At such a low alumina concentration, it is unlikely that a Q^n is coordinated to more than one AlO_4 tetrahedron. The effect of this coordination is to move the ^{29}Si chemical shift to a less negative value by ∼5 ppm. We do not expect the addition of 2% Al_2O_3 to have a large influence on the Cs^+ cation distribution in the cesium silicate glass. It is useful, however, to examine the effect of ^{27}Al, an NMR active nucleus, on the ^{29}Si MAS echo-train coherence lifetimes. The ^{27}Al nucleus is 100% abundant and has a $\gamma_I\hbar$ value that is ∼2 times larger than ^{133}Cs. In Fig. 3(E) is the 2D FT-ILT of the 7Cs:2Al:91Si glass composition. As expected, the modes of the isotropic chemical shifts for both Q^4 and Q^3 move to less negative values, as seen in Table 5. There is also a clear decrease in the shortest coherence lifetimes of both Q^4 and Q^3 with the addition of alumina compared to the 5Cs:95Si and 10Cs:90Si glasses. These shorter lifetimes are likely associated with $Q^{4,333A}$[1Al] and $Q^{3,33A}$[1Al], *i.e.*, the Q^n sites coordinated to one AlO_4 and Q^3 sites. There is also a slight increase in the longest coherence lifetimes of both Q^4 and Q^3 with the addition of alumina compared to the 10Cs:90Si glass. This is due to the decrease in the relative population of the Q^3 sites and an increase in the relative population of the $Q^{4,4444}$ sites. Overall, the addition of alumina leads to a slightly wider distribution of coherence lifetimes; however, there is only a slight increase in the ratio of r_λ = 1.7 using the mean Q^4 and Q^3 lifetimes from the cross-sections shown in Fig. 3(F).

3.2 Lithium silicate glasses

Now that we have established the behavior of ^{29}Si echo-train coherence lifetimes in non-phase separated glasses, we shift our attention to phase-separated glasses as indicated by surface imaging. The SEM images of the 5Li:95Si and 10Li:90Si glasses in Fig. 4(A) and (D), respectively, show the distinct occurrence of phase separation. In highly siliceous binary lithium silicate glasses, phase separation into a lithium-rich phase with about 33 mol% Li_2O and a lithium-poor domain is expected.[67] The spherical form of the volumetrically minor phase, which in all cases shown here is the phase with high alkali content, further indicates that phase separation occurs *via* the nucleation and growth mechanism.[27] The lithium-rich spheres reach diameters of up to 50 nm in the sample with 5% lithium oxide and greater than 200 nm in the sample with 10%. As noted earlier, the larger domains in the 10Li:90Si glass lead to a strong opalescence behavior, as shown in Fig. S1 of the ESI.† In contrast to the X-ray diffraction data (see Fig. S2 of the ESI†), there is no evidence of crystalline cristobalite in the ^{29}Si MAS spectrum of the 10Li:90Si glass, shown in Fig. 2(B). This is likely due to the longer ^{29}Si longitudinal relaxation times of crystalline silicate phases relative to silicate glasses.

The 2D FT-ILT ^{29}Si spectra of the phase-separated 5Li:95Si glass is shown in Fig. 4(B). The Q^4 sites at isotropic chemical

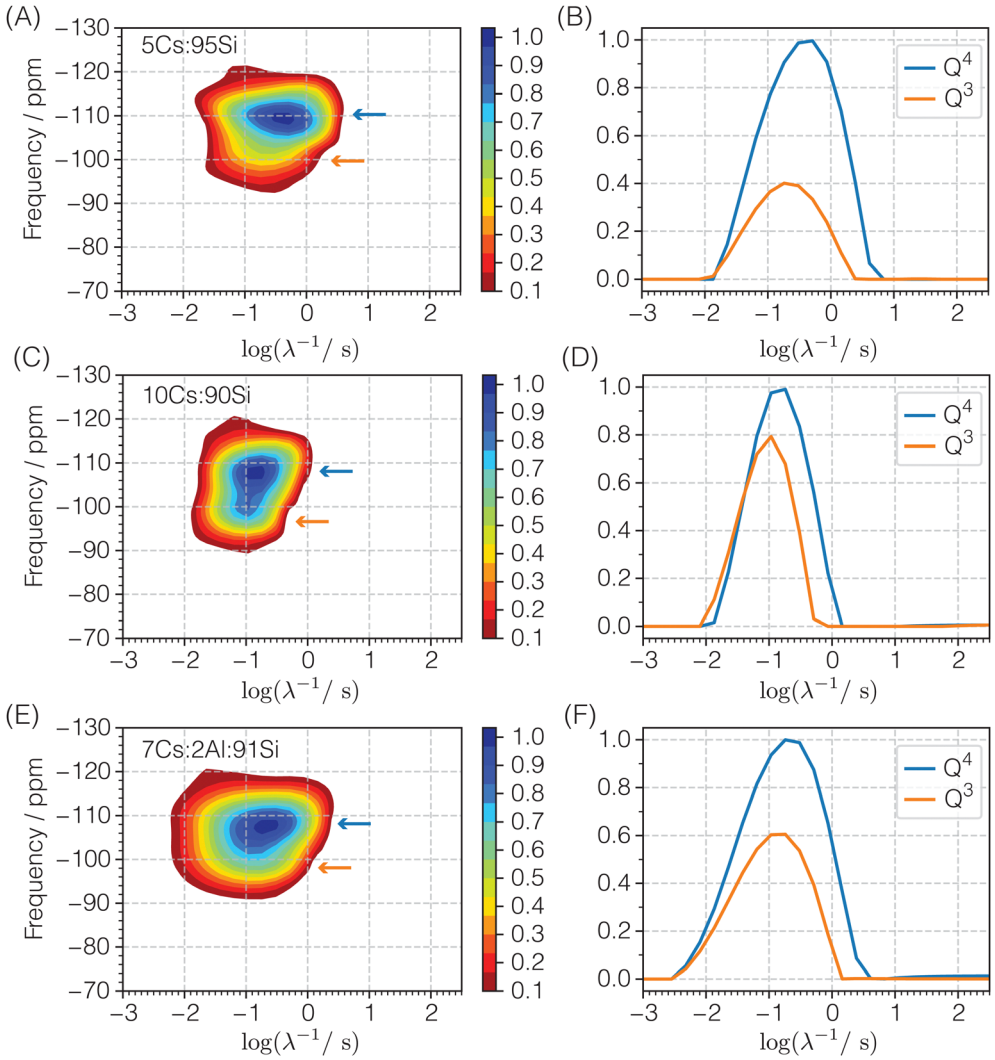

Fig. 3 The ^{29}Si 2D shifted-echo PIETA spectrum obtained from Fourier and inverse Laplace transforms for (A) 5Cs:95Si, (C) 10Cs:90Si and (E) 7Cs:2Al:91Si. The vertical axis is the spectroscopic (MAS) dimension, and the horizontal axis is the dimension associated with the logarithm of the echo-train coherence lifetime. Frequencies in ppm are referenced to TMS. Cross-sections along the coherence lifetime dimension through the maximum amplitude of Q^4 and Q^3 are shown for (B) 5Cs:95Si, (D) 10Cs:90Si, and (F) 7Cs:2Al:91Si. The isotropic chemical shifts of the cross-sections are indicated as arrows in (A), (C), and (E), respectively.

shifts around $\delta_{cs} = -111.5$ ppm have a distribution of coherence lifetimes that cover over three orders of magnitude inside the region of $\sim 10^{-2}$ s to $\sim 10^{2}$ s, peaking at a lifetime near $\lambda^{-1} = 862.0$ ms. In contrast, the Q^3 sites around $\delta_{cs} = -93.5$ ppm have a narrower distribution of coherence lifetimes, covering over one order of magnitude inside the region of $\sim 10^{-3}$ s to $\sim 10^{0}$ s, and peaking at a shorter lifetime near $\lambda^{-1} = 38.1$ ms. This dramatic difference is attributed to the phase separation of the glass. In this case, the shorter coherence lifetimes result from residual magnetic dipolar couplings to the lithium ions, which are significantly stronger for the Q^3 sites due to their closer proximity to the lithium ions in the lithium-rich phase with about 33 mol% Li_2O. Also, recall from eqn (6) that the stronger homonuclear dipolar couplings between ^{7}Li nuclei in the lithium-rich phase "amplify" the residual dipolar coupling to ^{29}Si. The Q^4 sites with shorter coherence lifetimes overlapping those of the Q^3 sites are likely part of the lithium-rich phase. The Q^4 sites with longer coherence lifetimes belong to the lithium-poor domain. As we saw in the cesium silicate glasses, in a non-phase separated sample where Li^+ is distributed homogeneously, one would expect all Q^n sites to be in relative proximity to the modifier cations and have more overlapping coherence lifetime distributions. Using the mean Q^4 and Q^3 lifetimes from the cross-sections taken at the modes of the Q^4 and Q^3 2D distributions, shown in Fig. 4(C), we obtain a ratio of $r_\lambda = 28.8$, *i.e.*, an order of magnitude larger than r_λ values observed in the non-phase separated cesium silicate glasses.

Phase separation is also distinguishable in the 2D FT-ILT spectrum of the 10Li:90Si glass, shown in Fig. 4(E). Compared to the 5Li:95Si glass, the Q^4 sites at isotropic chemical shifts around $\delta_{cs} = -109.0$ ppm have a smaller distribution of coherence lifetimes, covering over two orders of magnitude

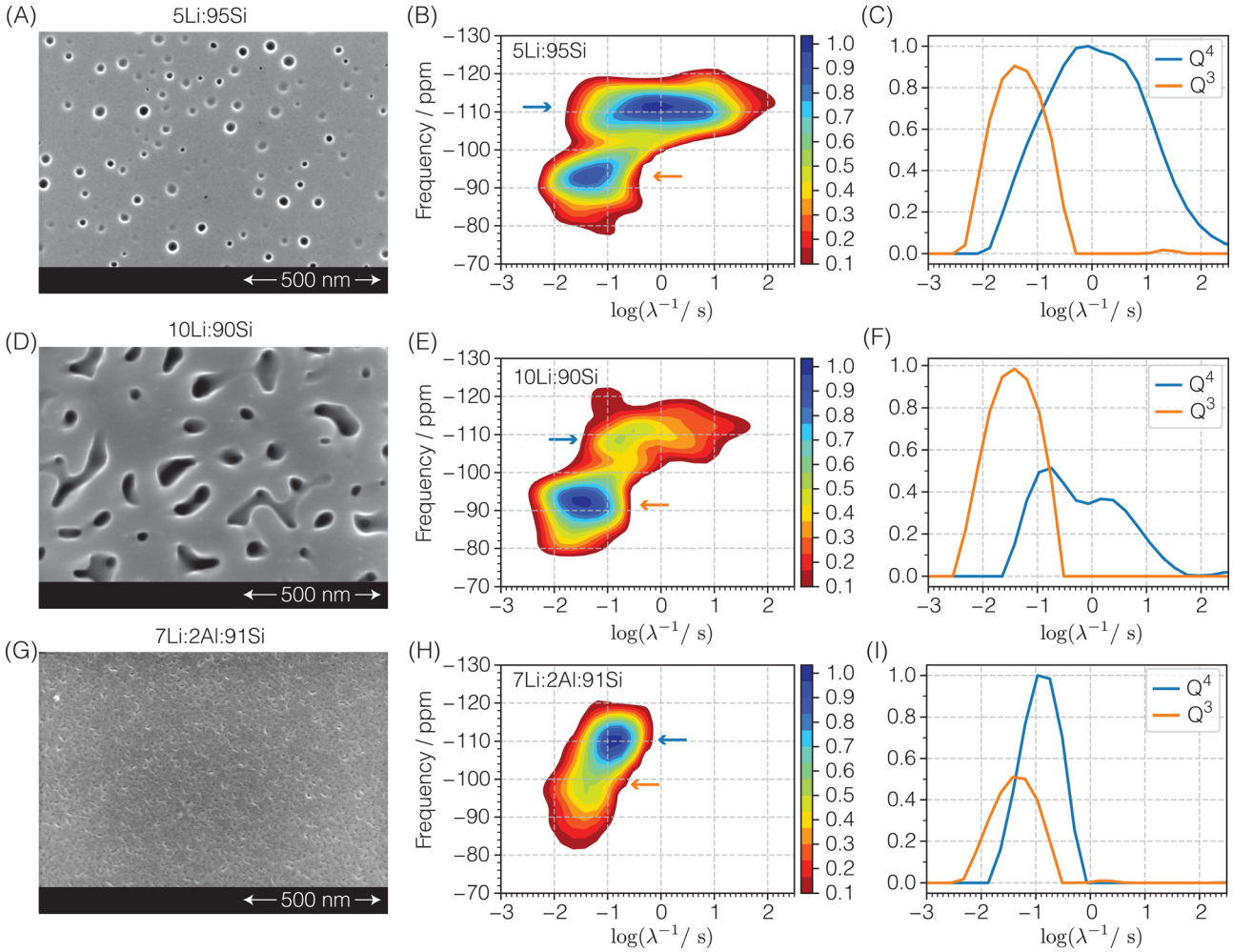

Fig. 4 SEM micrographs of (A) 5Li:95Si, (D) 10Li:90Si and (G) 7Li:2Al:91Si glasses after etching with 0.1% HF. The ^{29}Si 2D shifted-echo PIETA spectrum obtained from Fourier and inverse Laplace transforms for (B) 5Li:95Si, (E) 10Li:90Si and (H) 7Li:2Al:91Si. The vertical axis is the spectroscopic (MAS) dimension, and the horizontal axis is the dimension associated with the logarithm of the echo-train coherence lifetime. Frequencies in ppm are referenced to TMS. Cross-sections along the coherence lifetime dimension through the maximum amplitude of Q^4 and Q^3 are shown for (C) 5Li:95Si, (F) 10Li:90Si, and (I) 7Li:2Al:91Si. The isotropic chemical shifts of the cross-sections are indicated as arrows in (B), (E), and (H), respectively.

inside $\sim 10^{-2}$ s to $\sim 10^{2}$ s. In contrast, the Q^3 sites around δ_{cs} = −91.9 ppm still cover over one order of magnitude inside $\sim 10^{-3}$ s to $\sim 10^{0}$ s, and still peak at a lifetime near λ^{-1}= 38.1 ms. The relative invariance of the Q^3 coherence lifetime distribution suggests that the composition of the Li-rich phase remains constant (at 33% Li) while this phase grows in size. The growth of this Li-rich phase also reduces the probability of remote Q^4 sites, leading to the reduction of the longer Q^4 coherence lifetimes. In the Q^4 case, we also observe a bimodal distribution of coherence lifetimes with the highest intensity peaking around λ^{-1} = 181.2 ms and a slightly lower peak near λ^{-1} = 1.4 s. This is more clearly seen in the cross-sections taken at the modes of the Q^4 and Q^3 2D distributions, shown in Fig. 4(F). The bimodal Q^4 distribution is further evidence for phase separation in this glass composition, although the extension of the Q^4 coherence lifetime by two orders of magnitude beyond the longest Q^3 coherence lifetime more strongly supports this conclusion. The ratio of the mean coherence lifetimes for Q^4 and Q^3 is r_λ = 23.8.

The SEM micrograph for the 7Li:2Al:91Si sample, to which 2% Al_2O_3 was added, is shown in Fig. 4(G). The SEM micrograph shows that adding small amounts of alumina considerably changed the sample's morphology while not completely suppressing phase separation. Close observation of the SEM image still reveals the presence of two different domains. The size of the spheres of the minor phase is below 20 nm, but they appear in much larger quantities. Additionally, the contrast difference among both regions is lower, suggesting they are closer in chemical composition. The corresponding 2D FT-ILT spectrum of the 7Li:2Al:91Si sample is shown in Fig. 4(H). The coherence lifetimes of the Q^4 sites peak at λ^{-1} = 107.7 ms, considerably shorter compared to the samples without alumina, while the Q^3 site coherence lifetimes, peaking at λ^{-1} = 38.1 ms, remain relatively close to the Q^3 lifetimes in the 5Li:95Si and 10Li:90Si glasses.

From a least-squares fit of the ^{29}Si MAS spectra of the 7Li:2Al:91Si glass, shown in Fig. 2(C), we determine the modes of the Q^4 and Q^3 chemical shift distributions given in Table 5. Cross-sections as a function of coherence lifetime taken at the

respective modes of the Q^4 and Q^3 chemical shift distributions are shown in Fig. 4(I). The ratio of the mean coherence lifetimes for Q^4 and Q^3 in the 7Li:2Al:91Si sample is reduced to r_λ = 3.0. The coherence lifetime difference between the Q^3 and Q^4 sites is still appreciable, as Q^4 remain, on average, more distant from the lithium ions than the Q^3 in the 7Li:2Al:91Si glass. Nonetheless, the smaller gap between the Q^3 and Q^4 lifetimes indicates that the lithium poor and rich domains have similar amounts of lithium, *i.e.*, the Li distribution in this sample is more homogeneous than those without alumina. It should be stated that, in this context, by homogeneous, we refer to longer length scales. These results do not exclude the possibility of microsegregation (as the SEM images suggest), *i.e.*, cation clustering in channels or percolation thresholds at smaller length scales. Other NMR techniques may be better suited for studying such phenomena.[66]

3.3 Sodium and potassium silicate glasses

The SEM micrographs of the sodium and potassium silicate glasses are shown in Fig. 5(A) and (D), respectively. Two distinct phases are observed in the SEM image for the 5Na:95Si glass in Fig. 5(A), with sodium-rich spheres on the order of 20 nm, *i.e.*, five times smaller than the 5Li:95Si composition. The SEM image of the 5K:95Si glass in Fig. 5(D) does not show any feature that would indicate the presence of phase separation.

The 2D FT-ILT of the phase-separated 5Na:95Si glass is shown in Fig. 5(B). The Q^4 sites at isotropic chemical shifts around δ_{cs} = −110.7 ppm have a broad coherence lifetime distribution that covers over three orders of magnitude inside 10^{-2} to 10^{1}, peaking at a coherence lifetime near λ^{-1} = 181.2 ms. The Q^3 sites at δ_{cs} = −94.4 ppm have a narrower coherence lifetime distribution that covers over one order of magnitude inside 10^{-2} to 10^{0}, peaking at a coherence lifetime near λ^{-1} = 107.7 ms. The cross-sections as a function of coherence lifetime, taken through the modes of the 2D distribution, are shown in Fig. 5(C). From the mean lifetimes of the cross-section distributions for the phase-separated 5Na:95Si glass, shown in Fig. 5(C), we obtain a ratio of r_λ = 5.8. The r_λ ratio is significantly higher than the ratio found in the homogeneous glasses, in agreement with the presence of phase separation. It is lower than the ratio found in the phase-separated lithium silicate glasses, which is also consistent with the sodium silicates' lower tendency towards phase separation than the lithium silicates.

As noted earlier, we expect the isotropic chemical shifts of Q^4 sites to become less negative with an increasing amount of nearest neighbor Q^3 sites.[65,66] This is consistent with the observation of an increase in the intensity of the less negative chemical shifts at shorter coherence lifetimes of the Q^4 sites in Fig. 5(B).

The mean coherence lifetime for Q^4 in the 5Na:95Si glass is considerably shorter than the mean coherence lifetimes for Q^4 in the phase-separated 5Li:95Si and 10Li:90Si glasses. Given the higher $\gamma_I\hbar$ of ^{7}Li and the shorter ^{29}Si–^{7}Li and ^{7}Li–^{7}Li distances, this suggests a higher modifier cation concentration in the silica-rich phase of the 5Na:95Si glass compared to the phase-separated 5Li:95Si and 10Li:90Si glasses. It is also noteworthy

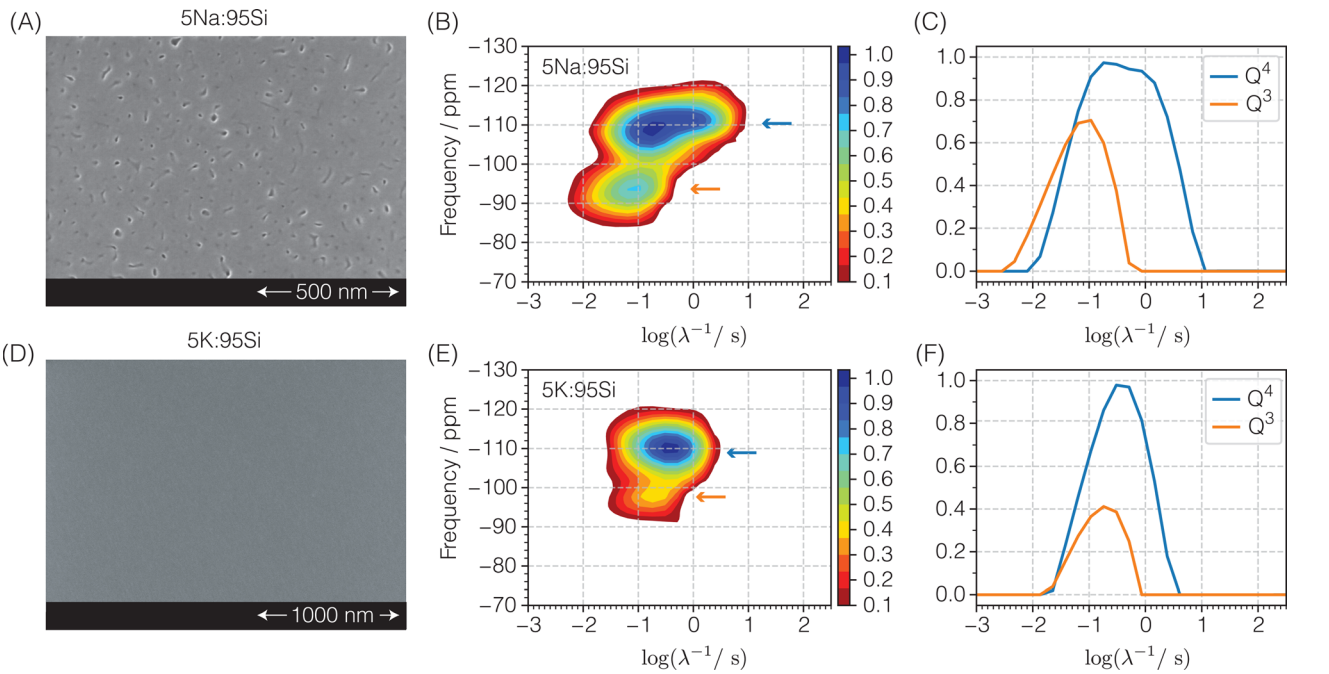

Fig. 5 SEM micrographs of (A) 5Na:95Si and (D) 5K:95Si glasses after etching with 0.1% HF. The ^{29}Si 2D shifted-echo PIETA spectrum obtained from Fourier and inverse Laplace transforms for (B) 5Na:95Si and (E) 5K:95Si. The vertical axis is the spectroscopic (MAS) dimension, and the horizontal axis is the dimension associated with the logarithm of the echo-train coherence lifetime. Frequencies in ppm are referenced to TMS. Cross-section along the coherence lifetime dimension through the modes of the Q^4 and Q^3 2D distributions are shown for (C) 5Na:95Si and (F) 5K:95Si. The isotropic chemical shifts of the cross-sections are indicated as arrows in (B) and (E), respectively.

that the ^{29}Si coherence lifetimes of Q^3 in the 5Na:95Si glass are longer than in the lithium silicate glasses. This is consistent with a lower modifier cation concentration in the sodium-rich phase of the phase-separated 5Na:95Si glass. However, it may also be due, in part, to the smaller $\gamma_I\hbar$ of the ^{23}Na compared to ^{7}Li.

The 2D FT-ILT of the 5K:95Si glass is shown in Fig. 5(E). The Q^4 sites at isotropic chemical shifts around $\delta_{cs} = -109.8$ ppm have a coherence lifetime distribution that covers two orders of magnitude inside 10^{-2} to 10^1, peaking at a coherence lifetime near $\lambda^{-1} = 304.7$ ms. The Q^3 sites at $\delta_{cs} = -98.4$ ppm have a narrower coherence lifetime distribution that covers one order of magnitude inside 10^{-2} to 10^0, peaking at a coherence lifetime near $\lambda^{-1} = 181.2$ ms. The cross-sections as a function of coherence lifetime, taken through the modes of the 2D distribution, are shown in Fig. 5(F). From these cross-sections, we obtain the mean lifetimes ratio of $r_\lambda = 2.1$ in the 5K:95Si glass, which appears to be consistent with the lack of any apparent phase separation in the SEM image of Fig. 5(D).

The $\gamma_I\hbar$ of ^{133}Cs is nearly a factor of three times larger than the ^{39}K cation (see Table 4). Thus, compared to the homogeneous potassium silicate glass, one might expect shorter coherence lifetimes for both Q^3 and Q^4 sites in the cesium silicate glasses. However, the mean coherence lifetime of 192.1 ms for Q^3 in the 5Cs:95Si glass is longer than the value of 151.4 ms found in the 5K:95Si glass. Additionally, the mean coherence lifetime of Q^4 is similar in both the 5Cs:95Si and 5K:95Si glasses, at $\sim$316 ms. This lengthening of the ^{29}Si coherence lifetimes in the cesium silicate glasses is a result of a further reduction in the residual heteronuclear dipolar coupling between ^{133}Cs and ^{29}Si due to a large ^{133}Cs chemical shift anisotropy, which arises from the greater number of electrons in the closed shell configuration of the cesium cation. This mechanism for eliminating residual dipolar couplings is well understood and can be particularly effective in paramagnetic samples.[68]

4 Summary

We have shown that differential echo-train coherence lifetimes of ^{29}Si nuclear magnetization can detect phase separation in silicate glasses, even at small scales where the glass appears optically homogenous. This approach relies on differences between residual heteronuclear dipolar couplings to ^{29}Si in the different phases. Most important, the residual ^{29}Si heteronuclear dipolar couplings to the NMR-active quadrupolar nuclides of the alkali cations are proportional to the size of the gyromagnetic ratio for the alkali cation nuclei with an inverse cubed dependence on the distances between alkali cations and the distances between the alkali cations and the ^{29}Si nuclides. The dependence of the residual coupling on the strong homonuclear couplings between the alkali cations in the alkali-rich phases makes this approach particularly sensitive to phase separation. These residual dipolar couplings remain the dominant dephasing mechanism of the ^{29}Si echo-train at MAS speeds yielding high-resolution ^{29}Si MAS spectra. With increasing MAS rates and higher rf field strengths, however, one may expect the residual heteronuclear dipolar couplings to ^{29}Si to be further reduced along with the ability to detect phase separation through echo-train coherence lifetime differences. Similarly, this approach may be less effective in glass compositions that are dilute in NMR active nuclei, such as alkaline earth silicate glasses, where the residual heteronuclear dipolar couplings to ^{29}Si are significantly weaker.

We also show in these measurements that the effects of J coupling modulations of the ^{29}Si echo train amplitudes can be eliminated through the use of shifted-echo PIETA, which acquires simultaneous $\mathbb{P}_{AX}$ and $(\mathbb{PP})_{AX}$ echoes at the beginning of the π-pulse echo train acquisition. This modified pulse sequence is particularly valuable when the echo-train coherence lifetimes span orders of magnitude.

To quantify the ^{29}Si echo-train coherence lifetimes, we employ an inverse Laplace transform[29] (ILT) with l_1 regularization as it provides a more quantitative and less restrictive analysis compared to a multi- or stretched exponential model. The additional correlation of the ILT of ^{29}Si echo-train decay to the high resolution ^{29}Si MAS spectrum gives insight into the local structure and composition of the distinct phases. Cognizant that such analyses for non-crystalline materials must become accessible to non-NMR specialists working in the field, we have also developed an open-source Python package for performing the inversion of echo-train acquisition solid-state NMR datasets into the distribution of echo-train coherence lifetimes.[60]

This approach complements the established NMR technique of differential paramagnetic relaxation enhancements to detect phase separation in glasses.[11–15] Indeed, with paramagnetic doping, one can envision the combination of both approaches, through the use of a 2D ILT,[29,69] to create a 3D dataset correlating longitudinal relaxation rates to echo-train decay rates to a resolved MAS spectrum, perhaps providing an even more sensitive tool for detecting phase separation in glasses.

Data availability

The open-source Python package, *mrinversion*, for implementing the TSVD–FISTA ILT described here along with documentation for its installation and use is made available in Zenodo at **https://doi.org/10.5281/zenodo.3964643**, ref. 60 The documentation for *mrinversion* also includes example scripts for obtaining inversions of all the experimental datasets presented in this work and synthetic datasets. The experimental CSDM[70] compliant datasets and Python notebooks that support the findings of this study are openly available in Zenodo at **https://doi.org/10.5281/zenodo.6974553**, ref. 71

Conflicts of interest

There are no conflicts to declare.

Appendix A: inverse laplace transform

The λ^{-1} distributions from the PIETA experiments were obtained through the Inverse Laplace Transform (ILT). Here,

we give a brief explanation of the mathematical procedures. Inversion problems involving Fredholm integrals of the first kind are frequently encountered in the field of NMR, especially in the inversion of relaxation measurements that determine longitudinal and transverse relaxation times and the correlation between them. In this study, we focus on the one-dimensional inversion of a distribution of π-pulse echo train coherence lifetimes where the NMR signal follows

$$s(t) = \int_{\lambda^{-1}} f\left(\lambda^{-1}\right) \exp\left(-\frac{t}{\lambda^{-1}}\right) \mathrm{d}\lambda^{-1} + e(t). \tag{10}$$

Here $s(t)$ is the measured signal with $e(t)$ noise and $f(\lambda^{-1})$ is the unknown λ^{-1} distribution to be determined. Because $s(t)$ is defined as a Laplace transformation of the distribution $f(\lambda^{-1})$, this particular type of inversion is commonly referred to as inverse Laplace transformation. When discretized, eqn (10) is approximated to

$$\mathbf{s} = \mathbf{K}\cdot\mathbf{f} + \mathbf{e}, \tag{11}$$

where $\mathbf{K} \in \mathbb{R}^{m\times n}$ is the Laplace matrix defined as $K_{ij} = \exp(-t_i/\lambda_j^{-1})$ and is called the kernel, $\mathbf{s} \in \mathbb{R}^m$ is the measured signal, $\mathbf{f} \in \mathbb{R}^n$ is the vector to be determined, and $\mathbf{e} \in \mathbb{R}^m$ is the measurement noise assumed to be white Gaussian with zero mean. The column vectors and m and n are the sampling size of the vectors $\mathbf{s}$ and $\mathbf{f}$, respectively.

The inverse Laplace Transformation is well known[72–77] to be an ill-conditioned problem. An ill-conditioned problem does not have a unique solution, and any small perturbation in the problem, *e.g.* the noise in signal $\mathbf{s}$, can lead to large fluctuations in the solution $\mathbf{f}$. To overcome this issue, regularization methods[72–77] are often implemented to stabilize the solution. The regularization term also called the 'penalty' term, is a measure of the 'irregularity' of the solution. In other words, a regularization simply replaces the original ill-conditioned problem with a ''nearby'' well-conditioned problem whose solution approximates the ''true'' solution of the original problem.

We implement a TSVD–FISTA hybrid algorithm in this work to regularize the inverse problem. Here TSVD and FISTA are the acronyms for Truncated Singular Value Decomposition and Fast Iterative Shrinkage Threshold Algorithm. For a given range of λ_j^{-1}'s, usually equally spaced on a logarithmic scale, the kernel K_{ij} is evaluated for time t_i's where t_i is the point correspondent to the signal $s(t_i)$. Having determined $\mathbf{K}$, the singular value decomposition of $\mathbf{K}$ follows,

$$\mathbf{K} = \mathbf{U}\cdot\mathbf{S}\cdot\mathbf{V}^{\mathrm{T}}, \tag{12}$$

where $\mathbf{U} \in \mathbb{R}^{m\times k}$ and $\mathbf{V} \in \mathbb{R}^{n\times k}$ are unitary matrices, $\mathbf{S} \in \mathbb{R}^{k\times k}$ is a diagonal matrix with non-negative real singular values, ς_i, arranged in decreasing order and $k = \min(m,n)$. For Laplace matrices, it is well known[74,78] that the singular values decay fast and that the smaller singular values are harmful. These smaller values are frequently discarded *via* truncation of singular values. We implement a maximum entropy[61,79,80] based method to determine the optimum truncation point r. Once r is determined, the inverse problem is projected onto a smaller subspace[29] to reduce the computational cost. In this subspace,

$$\tilde{\mathbf{K}} = \mathbf{S}_{\mathrm{r}}\cdot\mathbf{V}_{\mathrm{r}}^{\mathrm{T}}, \tag{13}$$

$$\tilde{\mathbf{s}} = \tilde{\mathbf{U}}^{\mathrm{T}}\cdot\mathbf{s}, \tag{14}$$

where $\tilde{\mathbf{K}} \in \mathbb{R}^{r\times n}$ is the ''nearby'' well-conditioned matrix, $\tilde{\mathbf{s}} \in \mathbb{R}^r$ is referred to as the compressed data and $\tilde{\mathbf{U}} \in \mathbb{R}^{m\times r}$, $\tilde{\mathbf{V}} \in \mathbb{R}^{n\times r}$, $\tilde{\mathbf{S}} \in \mathbb{R}^{r\times r}$ are the truncated matrices. The inverse problem in this subspace is further subjected to l_1 regularization[51–59] which minimizes the objective function

$$\mathbf{f}(\beta) = \underset{f>0}{\arg\min}\left(\underbrace{\left\|\tilde{\mathbf{K}}\cdot\mathbf{f} - \tilde{\mathbf{s}}\right\|_2^2}_{g(f)} + \beta\underbrace{\|\mathbf{f}\|_1}_{h(f)}\right), \tag{15}$$

where β is the Lagrangian multiplier, also called the regularization hyperparameter, which promotes sparsity in the solution. Here, the notations $\|\mathbf{x}\|_2^2 = \sum_i x_i^2$ and $\|\mathbf{x}\|_1 = \sum_i |x_i|$ denote the l_2 and l_1 norms, respectively, of a vector $\mathbf{x}$. Another important advantage of l_1-based regularization is that it is less sensitive to outliers in comparison with the l_2-based regularization.[52]

While $g(f)$ is a smooth continuously differentiable convex function, $h(f)$ is a convex function and not differentiable everywhere. Thus, eqn (15) has no analytical solution, and its solution must be computed numerically. The FISTA algorithm[52] is used to minimize the objective function, eqn (15). The stopping criterion is when the difference between the objective function at the ith and $(i+1)$th iteration levels off. Further information regarding this algorithm can be found in the paper by Beck and Teboulle.[52]

Our approach uses a stratified k-folds cross-validation method: the signal $\mathbf{s}$ is divided into k subsets of roughly equal size, $m_i \approx m/k$, called folds, where k is an integer number, typically chosen as 5 or 10. In addition, a range of hyperparameter values, in this case, $\beta \in \mathbb{R}_+^{n_\beta}$ are chosen on a uniform log scale, where the subscript + denotes positive numbers, and n_β are the total number of β values. Out of k folds, one fold is set aside and is called the test set. The remaining $(k-1)$ folds are collectively called the training set. In the following notation, we represent the ith test set with $\mathbf{s}^i$ and the corresponding training set with $\mathbf{s}^{-i}$. Similarly, the corresponding kernels are designated with $\mathbf{K}^i$ and $\mathbf{K}^{-i}$, respectively. For every training set, $\mathbf{s}^{-i}$, the model $\mathbf{f}_i(\beta)$ is evaluated following,

$$\mathbf{f}_i(\beta) = \underset{\mathbf{f}\geq 0}{\operatorname{argmin}}\left(\frac{1}{m-m_i}\left\|\mathbf{K}^{-i}\cdot\mathbf{f} - \mathbf{s}^{-i}\right\|_2^2 + \beta\|\mathbf{f}\|_1\right), \tag{16}$$

for the range of β values. Next, the mean square error (MSE), called the test error of the test set, is evaluated using

$$\varepsilon_i(\beta) = \frac{1}{m_i}\sum\left(\mathbf{K}^i\cdot\mathbf{f}_i(\beta) - \mathbf{s}^i\right)^2, \tag{17}$$

where the summation runs over the elements of the test set, $\mathbf{s}^i$. This process is repeated k times while assigning a different fold as the test set each time. The cross-validation error is then given as

$$\mathrm{CV}(\beta) = \frac{1}{m}\sum_{i=1}^{k} m_i\varepsilon_i(\beta). \tag{18}$$

The optimal $\beta^\star$ hyperparameter is determined as the argument

that minimizes the cross-validation error, given as

$$\beta^* = \arg\min_{\beta}\left(\left|\mathrm{CV}(\beta) - \sigma_e^2\right|\right), \quad (19)$$

where σ_e is the standard deviation of the noise.

Acknowledgements

This material is based upon work supported by the Chemical Measurement and Imaging program in the National Science Foundation Division of Chemistry under Grant No. CHE-1807922 and CHE-2107636 (with partial co-funding from the Ceramics program in the Division of Materials Research).

References

1 J. E. Shelby, *J. Am. Ceram. Soc.*, 1983, **66**, 754–757.
2 R. H. Doremus, *Glass Science*, John Wiley & Sons, Inc, New York, 2nd edn, 1994.
3 E. D. Zanotto, *Am. Ceram. Soc. Bull.*, 2010, **89**, 19–29.
4 W. Vogel, *Glass Chemistry*, Springer-Verlag, Berlin, 2nd edn, 1994.
5 P. F. James, *J. Mater. Sci.*, 1975, **10**, 1802–1825.
6 J. M. Howe, B. Fultz and S. Miao, *Characterization of Materials, Transmission Electron Microscopy*, John Wiley & Sons, Inc., Hoboken, NJ, USA, 2012, vol. 2, pp. 1063–1090.
7 D. N. Leonard, G. W. Chandler and S. Seraphin, *Characterization of Materials, Scanning Electron Microscopy*, John Wiley & Sons, Inc., Hoboken, NJ, USA, 2012, vol. 2, pp. 1050–1063.
8 B. R. Wheaton and A. G. Clare, *J. Non-Cryst. Solids*, 2007, **353**, 4767–4778.
9 J. Zarzycki and F. Naudin, *J. Non-Cryst. Solids*, 1969, **1**, 215–234.
10 C. J. Benmore, O. L. G. Alderman, S. R. Benmore, S. K. Wilke and R. J. K. Weber, *ACS Earth Space Chem.*, 2020, **4**, 1888–1894.
11 S. Sen and J. Stebbins, *Phys. Rev. B: Condens. Matter Mater. Phys.*, 1994, **50**, 822–830.
12 M. Mortuza, R. Dupree and D. Holland, *J. Non-Cryst. Solids*, 2001, **281**, 108–116.
13 J. F. Stebbins, N. Kim, M. J. Andrejcak, P. M. Boymel and B. K. Zoitos, *J. Am. Ceram. Soc.*, 2009, **92**, 68–74.
14 A. Hodroj, P. Simon, P. Florian, M.-H. Chopinet and Y. Vaills, *J. Am. Ceram. Soc.*, 2013, **96**, 2454–2460.
15 L. Martel, D. Massiot and M. Deschamps, *J. Non-Cryst. Solids*, 2014, **390**, 37–44.
16 N. Bloembergen, *Physica*, 1949, **15**, 386–426.
17 W. Blumberg, *Phys. Rev.*, 1960, **119**, 79–84.
18 W. J. Malfait, W. E. Halter and R. Verel, *Chem. Geol.*, 2008, **256**, 269–277.
19 F. Devreux, J. P. Boilot, F. Chaput and B. Sapoval, *Phys. Rev. Lett.*, 1990, **65**, 614–617.
20 G. B. Furman, E. M. Kunoff, S. D. Goren, V. Pasquier and D. Tinet, *Phys. Rev. B: Condens. Matter Mater. Phys.*, 1995, **52**, 10182–10187.
21 D. Jardón-Álvarez, M. O. Bovee and P. J. Grandinetti, *J. Magn. Reson.*, 2021, **333**, 107097.
22 P. Hudon and D. R. Baker, *J. Non-Cryst. Solids*, 2002, **303**, 299–345.
23 R. J. Charles, *J. Am. Ceram. Soc.*, 1966, **49**, 55–62.
24 Y. Gupta and U. Mishra, *J. Phys. Chem. Solids*, 1969, **30**, 1327–1334.
25 Y. Kawamoto and M. Tomozawa, *J. Am. Ceram. Soc.*, 1981, **64**, 289–292.
26 B. J. Moulton and G. S. Henderson, *Glasses: Alkali and Alkaline-Earth Silicates*, Elsevier, 2021, vol. 2, pp. 462–482.
27 J. E. Shelby, *Introduction to Glass Science and Technology*, Royal Society of Chemistry, 2005.
28 L. Martel, M. Allix, F. Millot, V. Sarou-Kanian, E. Véron, S. Ory, D. Massiot and M. Deschamps, *J. Phys. Chem. C*, 2011, **115**, 18935–18945.
29 L. Venkataramanan, Y. Q. Song and M. Hurlimann, *IEEE Trans. Signal Process.*, 2002, **50**, 1017–1026.
30 D. J. Srivastava, P. Florian, J. H. Baltisberger and P. J. Grandinetti, *Phys. Chem. Chem. Phys.*, 2018, **20**, 562–571.
31 D. Srivastava, J. Baltisberger, P. Florian, F. Fayon, R. Shakhovoy, M. Deschamps, N. Sadiki and P. Grandinetti, *Phys. Rev. B*, 2018, **98**, 134202.
32 E. A. Porai-Koshits, *J. Non-Cryst. Solids*, 1990, **123**, 1–13.
33 A. Wright, *J. Non-Cryst. Solids*, 1994, **179**, 84–115.
34 S. K. Lee and J. F. Stebbins, *Geochim. Cosmochim. Acta*, 2006, **70**, 4275–4286.
35 K. E. Kelsey, J. R. Allwardt and J. F. Stebbins, *J. Non-Cryst. Solids*, 2008, **354**, 4644–4653.
36 J. F. Stebbins, E. V. Dubinsky, K. Kanehashi and K. E. Kelsey, *Geochim. Cosmochim. Acta*, 2008, **72**, 910–925.
37 K. E. Kelsey, J. F. Stebbins, D. M. Singer, G. E. Brown, J. L. Mosenfelder and P. D. Asimow, *Geochim. Cosmochim. Acta*, 2009, **73**, 3914–3933.
38 S. K. Lee and J. F. Stebbins, *Geochim. Cosmochim. Acta*, 2009, **73**, 1109–1119.
39 L. M. Thompson and J. F. Stebbins, *Am. Mineral.*, 2011, **96**, 841–853.
40 M. Edén, *Annu. Rep. NMR Spectrosc.*, 2015, **86**, 237–331.
41 J. L. Markley, W. J. Horsley and M. P. Klein, *J. Chem. Phys.*, 1971, **55**, 3604–3605.
42 E. L. Hahn, *Phys. Rev.*, 1950, **80**, 580–594.
43 A. Hodroj, P. Simon, P. Florian, M.-H. Chopinet and Y. Vaills, *J. Am. Ceram. Soc.*, 2013, **96**, 2454–2460.
44 J. H. Baltisberger, B. J. Walder, E. G. Keeler, D. C. Kaseman, K. J. Sanders and P. J. Grandinetti, *J. Chem. Phys.*, 2012, **136**, 211104.
45 P. J. Grandinetti, J. T. Ash and N. M. Trease, *Prog. Nucl. Magn. Reson. Spectrosc.*, 2011, **59**, 121–196.
46 J. A. Aguilar, M. Nilsson, G. Bodenhausen and G. A. Morris, *Chem. Commun.*, 2012, **48**, 811–813.
47 K. Takegoshi, K. Ogura and K. Hikichi, *J. Magn. Reson.*, 1989, **84**, 611–615.
48 P. C. van Zijl, C. T. Moonen and M. von Kienlin, *J. Magn. Reson.*, 1990, **89**, 28–40.
49 H. Y. Carr and E. M. Purcell, *Phys. Rev.*, 1954, **94**, 630–638.

50 S. Meiboom and D. Gill, *Rev. Sci. Instrum.*, 1958, **29**, 688.
51 I. Daubechies, M. Defrise and C. De Mol, *Comm. Pure Appl. Math.*, 2004, **57**, 1413–1457.
52 A. Beck and M. Teboulle, *SIAM J. Imaging Sci.*, 2009, **2**, 183–202.
53 X. Zhou, G. Su, L. Wang, S. Nie and X. Ge, *J. Magn. Reson.*, 2017, **275**, 46–54.
54 P. D. Teal and C. Eccles, *Inverse Probl.*, 2015, **31**, 045010.
55 M. Urbańczyk, D. Bernin, W. Koźmiński and K. Kazimierczuk, *Anal. Chem.*, 2013, **85**, 1828–1833.
56 M. Urbańczyk, M. Nowakowski, W. Koźmiński and K. Kazimierczuk, *J. Biomol. NMR*, 2017, **68**, 155–161.
57 M. Urbańczyk and K. Kazimierczuk, 2013 Signal Processing Symposium (SPS), Serock, Poland, 2013.
58 M. Guerquin-Kern, J. Baritaux and M. Unser, ICASSP 2011-2011 IEEE International Conference on Acoustics, Speech and Signal Processing, Prague, Czech Republic, 2011.
59 M. Teboulle and A. Beck, *Convex Optimization in Signal Processing and Communications: Gradient-based algorithms with applications to signal-recovery problems*, Cambridge University Press, Cambridge, 2009, pp. 42–88.
60 D. Srivastava and P. J. Grandinetti, mrinversion: v0.1.0: A python package for statistical learning of NMR tensors from 2D isotropic/anisotropic correlation nuclear magnetic resonance spectra, *J. Chem. Phys.*, 2020, **153**(13), 134201, DOI: **10.5281/zenodo.3964643**.
61 D. J. Srivastava and P. J. Grandinetti, *J. Chem. Phys.*, 2020, **153**, 134201.
62 J. V. Smith and C. S. Blackwell, *Nature*, 1983, **303**, 223–225.
63 F. Mauri, A. Pasquarello, B. G. Pfrommer, Y.-G. Yoon and S. G. Louie, *Phys. Rev. B: Condens. Matter Mater. Phys.*, 2000, **62**, R4786–R4789.
64 F. Angeli, O. Villain, S. Schuller, S. Ispas and T. Charpentier, *Geochim. Cosmochim. Acta*, 2011, **75**, 2453–2469.
65 L. Olivier, X. Yuan, A. N. Cormack and C. Jäger, *J. Non-Cryst. Solids*, 2001, **293–295**, 53–66.
66 D. Jardón-Álvarez, K. J. Sanders, P. Phyo, J. H. Baltisberger and P. J. Grandinetti, *J. Chem. Phys.*, 2018, **148**, 094502.
67 B. M. Wright and J. E. Shelby, *Phys. Chem. Glasses*, 2000, **41**, 192–198.
68 Y. Ishii, N. P. Wickramasinghe and S. Chimon, *J. Am. Chem. Soc.*, 2003, **125**, 3438–3439.
69 Y. Q. Song, L. Venkataramanan, M. Hurlimann, M. Flaum, P. Frulla and C. Straley, *J. Magn. Reson.*, 2002, **154**, 261–268.
70 D. J. Srivastava, T. Vosegaard, D. Massiot and P. J. Grandinetti, *PLoS One*, 2020, **15**, e0225953.
71 M. O. Bovee, D. Jardón-Álvarez, D. Srivastava, J. Wu and P. J. Grandinetti, *Phase separation in alkali silicate glasses detected through inverse Laplace transform of ^{29}Si π-pulse echo train decay*, 2022, DOI: **10.5281/zenodo.6974553**.
72 M. E. Kilmer and D. P. O'Leary, *SIAM J. Matrix Anal. Appl.*, 2001, **22**, 1204–1221.
73 A. N. Tikhonov and V. Y. Arsenin, *Solution of ill-posed problems*, Wiley, New York, 1977.
74 Y. Q. Song, L. Venkataramanan and L. Burcaw, *J. Chem. Phys.*, 2005, **122**, 104104.
75 J. Zwanziger, *Solid State Nucl. Magn. Reson.*, 1994, **3**, 219–229.
76 K. J. Dunn and G. A. LaTorraca, *J. Magn. Reson.*, 1999, **140**, 153–161.
77 W. Wang, P. Li and C. Ye, *Sci. China, Ser. A: Math., Phys., Astron.*, 2001, **44**, 1477–1484.
78 P. C. Hansen, *BIT Numer. Math.*, 1987, **27**, 534–553.
79 R. Varshavsky, A. Gottlieb, M. Linial and D. Horn, *Bioinformatics*, 2006, **22**, e507–e513.
80 X. Ge, H. Chen, Y. Fan, J. Liu, J. Cai and J. Liu, *Comput. Phys. Commun.*, 2017, **212**, 82–89.